Research Square

Preprints are preliminary reports that have not undergone peer review.
They should not be considered conclusive, used to inform clinical practice,
or referenced by the media as validated information.

Evo-TGSF: An Evolutionary Topology-Genomic Subspace Fusion Framework for Alzheimer's Disease Classification using Imaging-Genomics Data

Luyun Wang

188688767850163.com

Hangzhou Polytechnic University

Li Huang

Hangzhou Polytechnic University

Weidong Chen

Hangzhou Polytechnic University

Research Article

Keywords: Alzheimer's disease, disease diagnosis, fusion framework, imaging genomics, improved cuckoo–catfish optimizer

Posted Date: June 15th, 2026

DOI: https://doi.org/10.21203/rs.3.rs-9920004/v1

License: This work is licensed under a Creative Commons Attribution 4.0 International License.
Read Full License

Additional Declarations: No competing interests reported.

Evo-TGSF: An Evolutionary Topology-Genomic Subspace Fusion Framework for Alzheimer's Disease Classification using Imaging-Genomics Data

Abstract

Brain imaging genomics offers a powerful paradigm for unraveling the complex pathophysiological mechanisms underlying Alzheimer's disease (AD). However, effective integration of high-dimensional functional magnetic resonance imaging (fMRI) data and single nucleotide polymorphism (SNP) data remains challenging. In this paper, we propose an evolutionary topology-genomic subspace fusion framework, termed Evo-TGSF, for three-class and four-class Alzheimer's disease classification using fMRI and SNP data. First, we design a topology-augmented graph convolutional network (TA-GCN) for the fMRI modality, in which node representations are initialized using nine graph-theoretic measures derived from the brain connectivity toolbox. Second, we introduce a genomic subspace interaction network (GSI-Net) for the genomics modality, which employs a subspace tokenization strategy to project unordered SNP profiles into latent functional tokens, enabling the modeling of macroscopic epistatic interactions through self-attention mechanisms. Subsequently, we design an adaptive cross-modal gated fusion (ACM-GF) module, achieving the effective synthesis of heterogeneous features. Finally, to optimize the parameters, we propose an improved cuckoo–catfish optimizer (ICCO). Experimental results on the ADNI dataset demonstrate that Evo-TGSF framework achieves classification accuracies of 82.1%, 92.2%, 83.4%, 88.7% and 80.2% for HC/EMCI/LMCI, HC/EMCI/AD, EMCI/LMCI/AD, HC/LMCI/AD and HC/EMCI/LMCI/AD, respectively.

Keywords: Alzheimer's disease, disease diagnosis, fusion framework, imaging genomics, improved cuckoo–catfish optimizer

1 Introduction

Alzheimer's disease (AD) is a progressive neurodegenerative disorder characterized by a gradual decline in cognitive function [1, 2]. As a primary form of geriatric dementia, AD remains a critical focal point of global public health research. In recent years, driven by continuous advancements in neuroimaging and bioinformatics, the research

paradigm for AD has shifted from a reliance on single-modality data analysis toward a multimodal brain-imaging genomics approach.

Traditional studies have focused predominantly on single modalities, such as neuroimaging, to extract functional connectivity features for identifying disease-related brain regions [3]. However, due to the failure to integrate genomic variation information, it remains challenging to comprehensively capture the multidimensional features of the disease. Conversely, brain-imaging genomics achieves a cross-modal joint analysis from genetic variation to brain functional phenotypes by fusing functional magnetic resonance imaging (fMRI) and genomics data [4, 5]. This approach facilitates the elucidation of potential links between genetic regulatory mechanisms and neural circuit abnormalities. Researchers have proposed various optimization methods based on deep learning and multimodal fusion, which have enhanced the accuracy and robustness of AD-assisted diagnosis while demonstrating the effectiveness of diverse algorithms in clinical identification [6–8].

fMRI provides important information about functional interactions among brain regions and has been widely used to construct brain connectivity networks for AD diagnosis [9, 10]. In graph-based fMRI analysis, brain regions are represented as nodes and functional connections are modeled as edges. Graph neural networks, especially graph convolutional networks (GCN) [11, 12], have shown strong potential in learning discriminative representations from such brain networks. However, fMRI-derived functional connectivity matrices are often binarized to suppress weak and noisy connections, which may lead to the loss of connection strength information. As a result, standard GCN using simple node initialization strategies may not fully exploit the intrinsic topological properties of binary brain networks. In addition to neuroimaging data, single nucleotide polymorphism (SNP) data provide genetic susceptibility information associated with AD [13]. Imaging-genomics analysis enables the joint modeling of genetic variations and brain functional phenotypes, offering a more comprehensive perspective for understanding AD-related pathological changes. Nevertheless, SNP data are high-dimensional, discrete, and highly heterogeneous. Existing studies often treat SNPs as independent variables or rely on conventional feature selection methods, which limits their ability to capture high-order and non-linear interactions among genetic loci [14–16]. Therefore, developing an effective genomic representation learning strategy remains a key challenge in multimodal AD classification.

Another important challenge lies in the fusion of heterogeneous imaging and genomic modalities. Simple feature concatenation may introduce redundant information and fail to dynamically balance the contributions of different modalities [17, 18]. In AD diagnosis, fMRI features usually reflect current functional alterations, whereas SNP features represent relatively stable genetic risk factors. Their contributions may vary across subjects and diagnostic tasks. Therefore, an adaptive fusion mechanism is needed to model complementary information and assign appropriate modality weights in a data-driven manner. Meanwhile, the performance of multimodal deep learning models is highly affected by hyperparameter configurations, making automatic and robust optimization essential for improving generalization.

To address these challenges, this paper proposes the evolutionary topology-genomic subspace fusion framework (Evo-TGSF) for multi-class AD classification using fMRI

and SNP data. The topology-augmented graph convolutional network (TA-GCN) incorporates graph-theoretical priors to enhance fMRI-based binary brain network representation, while the genomic subspace interaction network (GSI-Net) projects high-dimensional SNP profiles into latent genomic subspace tokens and models their interactions through self-attention. The learned imaging and genomic features are then adaptively integrated by adaptive cross-modal gated fusion (ACM-GF), and multi-strategy improved cuckoo catfish optimizer algorithm (ICCO) is used to optimize key hyperparameters for improved classification stability.

The main contributions of this paper are summarized as follows:

- Novel feature encoding mechanisms are constructed to address the specific characteristics of heterogeneous modalities. For fMRI data, the TA-GCN is established to compensate for information loss in binary networks using BCT topological priors. For SNP data, the GSI-Net is designed to capture non-linear epistasis via a subspace tokenization strategy.
- Based on the proposed encoding mechanisms, the Evo-TGSF framework is developed. First, ICCO is employed to optimize key hyperparameters of Evo-TGSF, thereby improving the stability and generalization ability of the proposed framework. Second, the ACM-GF module is utilized to dynamically recalibrate the contribution weights of heterogeneous features, achieving high-confidence multimodal complementarity.
- We validate the performance of Evo-TGSF in disease classification and pathogenicity extraction using fMRI and SNP data obtained from the ADNI dataset. The results show that Evo-TGSF outperforms advanced methods in multi-class classification tasks. In addition, Evo-TGSF can precisely extract diseased brain regions and risk genes associated with AD progression.

2 Related Work

2.1 Graph Neural Networks for AD Diagnosis

Graph neural networks have been widely used in Alzheimer's disease diagnosis because brain imaging data can be naturally represented as graph-structured data. Compared with conventional vector-based machine learning methods, graph neural networks can directly learn topological patterns from brain networks and capture interactions among distributed brain regions. Peng *et al.* modeled synchronous correlations of blood oxygenation level dependent (BOLD) signals to construct a brain region network and employed GCN to learn synchronous brain connectivity patterns from the network and fused features [19]. Bi *et al.* proposed a feature aggregation GCN to model brain region–gene interactions via node-level feature aggregation, enabling effective characterization of Alzheimer's disease progression patterns [20]. Lei *et al.* developed a multi-scale enhanced graph convolutional network for MCI detection by jointly integrating structural features from diffusion tensor imaging and functional features from resting-state fMRI, where the outputs of multiple GCN layers are concatenated via a fully connected layer for disease classification [17]. Although these methods have shown promising performance, most existing GCN-based approaches rely heavily on the

adjacency matrix and use random initialization, one-hot encoding, or simple regional attributes as node features. In fMRI brain network analysis, functional connectivity matrices are often thresholded into binary graphs to reduce noise and emphasize network topology. However, this process may discard important connection strength information and make the graph representation sparse.

2.2 Multimodal Imaging-genomics Fusion

Brain imaging genomics provides a powerful framework for exploring the association between genetic variations and brain functional phenotypes in Alzheimer's disease. Neuroimaging data, such as fMRI and MRI, can reflect functional or structural alterations in the brain, while SNP data provide genetic susceptibility information related to disease progression. Recent studies have shown that integrating imaging and genetic data can improve diagnostic performance and provide complementary information for biomarker discovery [4, 5]. Jiao *et al.* proposed a deep autoencoder and self-representation network for multimodal imaging-genetics fusion, demonstrating the potential of deep representation learning for AD diagnosis and biomarker extraction [6]. Other studies have also explored multimodal deep learning frameworks by combining neuroimaging, clinical, and genetic information to improve the robustness of AD classification [7]. However, many existing methods still lack an adaptive mechanism to dynamically balance the contribution of imaging and genomic features for different subjects.

2.3 Metaheuristic Optimization in Medical Diagnosis

Metaheuristic optimization algorithms have been increasingly applied to medical diagnosis tasks, particularly for feature selection, hyperparameter tuning, and classifier optimization. Compared with manual parameter tuning or grid search, population-based optimization methods can perform global search in complex and non-convex solution spaces. Several studies have demonstrated the effectiveness of swarm intelligence algorithms in AD diagnosis. Sheng *et al.* presented a hybrid model combining an enhanced Harris Hawks Optimization algorithm with a kernel extreme learning machine. Their framework achieved simultaneous feature selection and classification across magnetic resonance imaging (MRI), positron emission tomography (PET) and cerebrospinal fluid (CSF) modalities, thus improving the performance of AD-assisted diagnosis [21]. Zhang *et al.* proposed an improved harris hawks optimization algorithm that integrates crisscross search and adaptive β-hill climbing to optimize a ResNet18-based deep learning model for Alzheimer's disease diagnosis, achieving superior classification performance across AD, mild cognitive impairment (MCI), and age-matched healthy controls (HC) groups [22]. Cui *et al.* introduced an adaptive LASSO logistic regression model optimized by particle swarm optimization, known as PSO-ALLR, to enhance AD classification performance based on MRI imaging features [23] . Lu *et al.* proposed a hybrid approach that integrates an improved binary salp swarm algorithm with a fuzzy K-nearest neighbor classifier for early AD diagnosis. This method used multimodal neuroimaging data, including MRI, PET and CSF biomarkers, to discriminate between subjects with MCI, AD, and HC [24]. Although

these optimization-based methods have improved diagnostic performance, they may still suffer from premature convergence, insufficient population diversity, or limited local exploitation ability.

3 Methods

3.1 Problem Formulation

Let $\mathcal{D} = \{(G_i, S_i, y_i)\}_{i=1}^{N}$ denoted the multimodal dataset, where G_i denotes the fMRI brain graph, S_i denotes the SNP vector, and y_i denotes the diagnostic label, the objective is to learn a multimodal mapping function to predict the disease stage.

3.2 Overall Framework

As shown in Figure 1, Evo-TGSF is a multimodal learning framework designed for three-class and four-class Alzheimer's disease classification by integrating topological brain priors and latent genomic subspace interactions. The framework separately extracts topology-augmented fMRI representations and phenotype-associated genomic features through a dual-stream architecture. These heterogeneous features are then adaptively integrated using a cross-modal gated fusion mechanism, while ICCO is introduced to optimize key model hyperparameters.

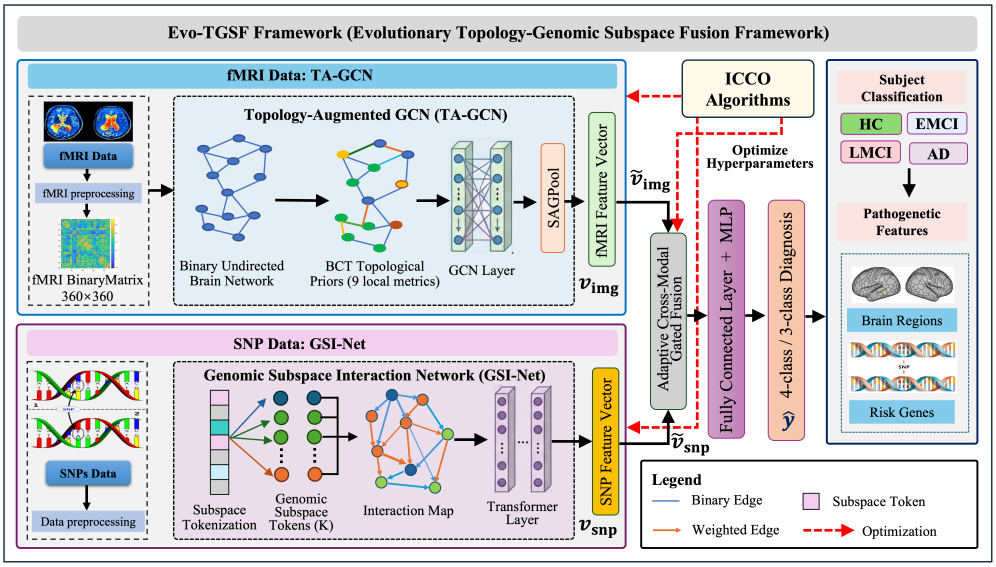


Fig. 1 The overall framework of our proposed Evo-TGSF model.

3.3 Topology-augmented Graph Learning for fMRI Data

For the brain imaging modality, we defined a graph $G = (\mathcal{V}, \mathbf{A}_{\text{bin}}, \mathbf{X}_{\text{bct}})$. Here, $\mathcal{V}$ represented the set of 360 regions of interest (ROIs), and $\mathbf{A}_{\text{bin}} \in \{0,1\}^{360\times360}$ was the binary adjacency matrix representing the functional connectivity. To incorporate domain knowledge, we utilized the brain connectivity toolbox (BCT) [25] to compute nine topological metrics for each node (e.g., strength, degree, clustering coefficient, local efficiency, betweenness centrality, eigenvector centrality, subgraph centrality, flow coefficient, and PageRank centrality). These metrics were reshaped into a node feature matrix $\mathbf{X}_{\text{bct}} \in \mathbb{R}^{360\times9}$, which served as the topological prior to initialize the graph network. To ensure feature comparability and numerical stability, all topological metrics were normalized to the range of $[-1, 1]$.

To effectively learn representations from binary adjacency matrix, we proposed the topology-augmented graph convolutional network module. Unlike standard GCNs that often used random initialization or one-hot encoding, our model explicitly leveraged $\mathbf{X}_{\text{bct}}$.

The layer-wise propagation rule was defined as

$$\mathbf{H}^{(l+1)} = \sigma(\tilde{\mathbf{D}}^{-\frac{1}{2}}\tilde{\mathbf{A}}_{\text{bin}}\tilde{\mathbf{D}}^{-\frac{1}{2}}\mathbf{H}^{(l)}\mathbf{W}^{(l)}_{\text{gcn}}), \tag{1}$$

where $\tilde{\mathbf{A}}_{\text{bin}} = \mathbf{A}_{\text{bin}} + \mathbf{I}_N$ was the adjacency matrix with self-loops, $\tilde{\mathbf{D}}$ denoted the corresponding degree matrix, and $\mathbf{W}^{(l)}_{\text{gcn}}$ was the learnable weight matrix. Crucially, we initialized the node representations as $\mathbf{H}^{(0)} = \mathbf{X}_{\text{bct}}$. This design enabled the network to propagate intrinsic topological properties across the functional connectivity matrix, thereby enriching the semantic representation of sparse binary connections.

To eliminate redundant ROIs and identify pathogenic hubs, we employed a self-attention pooling mechanism. A scoring vector Z was computed to measure nodal importance,

$$\mathbf{Z} = \sigma(\tilde{\mathbf{D}}^{-\frac{1}{2}}\tilde{\mathbf{A}}_{\text{bin}}\tilde{\mathbf{D}}^{-\frac{1}{2}}\mathbf{H}^{(L)}\mathbf{W}_{\text{att}}), \tag{2}$$

$$\text{idx} = \text{top-rank}(Z,\ \lfloor k \cdot N \rfloor), \tag{3}$$

$$\mathbf{H}_{\text{pooled}} = \mathbf{H}^{(L)}_{\text{idx},:} \odot \mathbf{Z}_{\text{idx}}, \tag{4}$$

where W_{att} denoted the learnable projection vector for estimating node importance scores, and top-rank$(\cdot)$ selected the top k nodes with the highest importance scores.

The pooled graph feature v_{img} was obtained via a readout operation combining global max and mean pooling,

$$v_{\text{img}} = \text{Concat}(\text{MeanPool}(\mathbf{H}_{\text{pooled}}), \text{MaxPool}(\mathbf{H}_{\text{pooled}})). \tag{5}$$

3.4 Genomic Subspace Interaction Network for SNP Data

For the genomic data, $\mathbf{S} \in \{0,1,2\}^M$ represented the SNP sequence with $M = 2318$, where values denoted the genotype. Thus, we treated $\mathbf{S}$ as an unordered set due to the absence of chromosomal coordinate information. We proposed a feature tokenization strategy to model the genomic profile as a set of latent functional subspaces, and

projected $\mathbf{S}$ into N_t latent tokens using a learnable transformation matrix $W_{\text{proj}} \in \mathbb{R}^{M \times (N_t \cdot d)}$:

$$\mathbf{T} = \text{Reshape}(\mathbf{S} \cdot W_{\text{proj}}), \tag{6}$$

where $\mathbf{T} \in \mathbb{R}^{N_t \times d}$ represented N_t genomic subspace tokens, each with dimensionality d. Each token represented a data-driven latent genomic subspace rather than a predefined biological pathway.

To capture the high-order non-linear interactions between these functional subspaces (i.e., macroscopic epistasis), we applied a Transformer Encoder on the generated tokens $\mathbf{T}$. Specifically, we computed the Query (Q_s), Key (K_s), and Value (V_s) matrices,

$$Q_s = \mathbf{T}W_{Q_s}, \quad K_s = \mathbf{T}W_{K_s}, \quad V_s = \mathbf{T}W_{V_s}. \tag{7}$$

The inter-subspace interaction was modeled using the scaled dot-product attention,

$$\text{Attn}(Q_s, K_s, V_s) = \text{Softmax}\left(\frac{Q_s K_s^{\mathsf{T}}}{\sqrt{d}}\right) V_s, \tag{8}$$

$$\mathbf{T}_{\text{updated}} = \text{FeedForward}(\text{LayerNorm}(\mathbf{T} + \text{Attn})). \tag{9}$$

The resulting attention map $\mathcal{A} \in \mathbb{R}^{N_t \times N_t}$ quantified the synergy between functional subspaces.

After L layers of adaptive interaction learning, the updated tokens contain rich context-aware genomic information. To obtain a compact representation for the final fusion stage, we aggregated the token set using Global Average Pooling [26],

$$v_{\text{snp}} = \frac{1}{N_t} \sum_{n_t=1}^{N_t} \mathbf{T}_{\text{updated}}^{(n_t)}, \tag{10}$$

where $v_{\text{snp}} \in \mathbb{R}^d$ served as the final genomic signature of the subject, ready to be fused with the brain imaging features.

3.5 Adaptive Cross-modal Gated Fusion

To eliminate the heterogeneity between multimodal representations, we first project features from different modalities into a shared latent space with dimension D_{fusion},

$$\tilde{v}_{\text{img}} = \text{ReLU}(v_{\text{img}}\mathbf{W}_1), \qquad \tilde{v}_{\text{snp}} = \text{ReLU}(v_{\text{snp}}\mathbf{W}_2), \tag{11}$$

where $\mathbf{W}_1$ and $\mathbf{W}_2$ were learnable linear projection matrices. The ReLU activation function introduced non-linear representational capability.

To dynamically balance the contribution of phenotypic (brain) and genotypic (SNP) features, we designed a gate-controlled fusion module. First, features were projected to a unified dimension d_f. Then, a gating coefficient $\alpha \in [0, 1]$ was learned,

$$\boldsymbol{\alpha} = \text{sigmoid}(\mathbf{W}_z[\tilde{v}_{\text{img}}, \tilde{v}_{\text{snp}}] + \mathbf{b}_z). \tag{12}$$

where α is defined as a sample-specific scalar gate, representing the relative contribution of fMRI and SNP modalities

The fused representation v_{final} was a weighted combination,

$$v_{\text{final}} = \boldsymbol{\alpha} \cdot \tilde{v}_{\text{img}} + (1 - \boldsymbol{\alpha}) \cdot \tilde{v}_{\text{snp}}. \tag{13}$$

Finally, the fused feature was fed into a multilayer perceptron (MLP) classifier to predict the disease stage [27],

$$\hat{y} = \text{Softmax}\left(\text{MLP}(v_{\text{final}})\right), \tag{14}$$

where $\hat{y}$ represented the predicted probability distribution over three or four diagnostic classes (HC, EMCI, LMCI and AD).

3.6 ICCO-based Hyperparameter Optimization

To improve the stability and generalization ability of Evo-TGSF, an improved cuckoo catfish optimizer (ICCO) was adopted to automatically search for the optimal hyperparameter configuration of the proposed framework. The original cuckoo catfish optimizer (CCO) was a population-based metaheuristic algorithm inspired by the cooperative hunting and brood-parasitic behaviors of cuckoo catfish. However, the original CCO might suffer from premature convergence when solving high-dimensional and non-convex optimization problems. To address this limitation, ICCO integrates three complementary strategies, including the algorithm introduced the nonlinear dynamic capture factor (NDCF), the elite differential mutation strategy (EDM), and the lens opposition-based learning (LOBL) mechanism [28].

In ICCO, each individual in the population represents a candidate hyperparameter configuration of Evo-TGSF. The optimization variables include the learning rate, L_2 regularization coefficient, hidden dimension of the TA-GCN module, number of genomic subspace tokens in GSI-Net, and fusion dimension of the ACM-GF module. For the i-th individual, its position vector was defined as

$$X_i = [lr, \lambda, d_{\text{gcn}}, N_t, d_f], \tag{15}$$

where lr denoted the learning rate, λ denoted the $L2$ regularization coefficient, d_{gcn} denoted the hidden dimension of TA-GCN, N_t denoted the number of genomic subspace tokens, and d_f denoted the shared fusion dimension.

The population is first initialized within the predefined search space,

$$x_{i,d}^0 = L_d + \text{rand}(0,1) \times (U_d - L_d), \quad d = 1, 2, \ldots, D, \tag{16}$$

where L_d and U_d denoted the lower and upper bounds of the $d-th$ dimension, respectively. For each candidate solution, Evo-TGSF was trained on the training subset and evaluated on the validation subset. The fitness function was defined as

$$\text{Fitness}(X_i) = 1 - \text{MacroF1}_{\text{val}}(X_i), \tag{17}$$

where $\mathrm{MacroF1}_{\mathrm{val}}$ was the macro-averaged F1-score on the validation set. A lower fitness value indicated a better hyperparameter configuration. Macro-F1 was used rather than accuracy because the ADNI2 cohort contains imbalanced diagnostic groups.

To balance global exploration and local exploitation, ICCO introduced a nonlinear dynamic capture factor,

$$C(t) = \cos\left(\frac{\pi t}{2T_{\max}}\right), \tag{18}$$

where t denoted the current iteration and $T_{\max}$ was the maximum number of iterations. Compared with the linear control strategy in the original CCO, this nonlinear schedule maintained stronger exploration in the early stage and gradually enhances exploitation in the later stage.

Second, an elite differential mutation strategy was incorporated to improve population diversity. When the population became over-concentrated around the current best solution, a new candidate was generated by

$$X_i^{t+1} = X_{\mathrm{best}}^t + r(X_{r1}^t - X_{r2}^t), \tag{19}$$

where X_{best}^t was the current best individual, X_{r1}^t and X_{r2}^t were two randomly selected individuals, and r was a random coefficient. This strategy enabled ICCO to explore new promising regions while retaining elite guidance.

Third, lens opposition-based learning was used to further enhance the ability to escape local optima. For the current best solution, an opposite candidate was generated as

$$X_{\mathrm{LOBL}} = \frac{U+L}{2} + \frac{U+L}{2k(t)} - \frac{X_{\mathrm{best}}}{k(t)}, \tag{20}$$

where $k(t) = 1 + (t/T_{\max})^{1/2}$ was the dynamic lens scaling factor. If the opposite candidate achieved a better fitness value, it replaced the current best solution.

After each update, boundary handling was applied to ensure that all candidate solutions remained within the predefined search ranges. Greedy selection was then used to retain the solution with the lower validation fitness. The optimization process terminated when the maximum number of iterations was reached or the validation fitness no longer improves. The best hyperparameter configuration obtained by ICCO was finally used to train Evo-TGSF for AD classification. The hyperparameter search space optimized by ICCO is summarized in Table 1.

Table 1 Search space of ICCO for optimizing Evo-TGSF

Hyperparameter	Search range	Type
Learning rate	$[10^{-5}, 10^{-2}]$	continuous
L_2 regularization	$[10^{-6}, 10^{-2}]$	continuous
TA-GCN hidden dimension	$\{32, 64, 128\}$	discrete
SNP token number	$\{8, 16, 32, 64\}$	discrete
Fusion dimension	$\{64, 128, 256\}$	discrete

The complete pipeline of the proposed Evo-TGSF framework was shown in Algorithm 1.

Algorithm 1 The procedure of Evo-TGSF framework

Input: fMRI data $\mathbf{G}$, SNP data $\mathbf{S}$, diagnostic labels $\mathbf{Y}$; ICCO search space Ω, population size P, maximum iterations $T_{\max}$.

Output: Predicted diagnostic labels $\hat{\mathbf{Y}}$ and optimized Evo-TGSF model.

Construct binary brain networks $\mathbf{A}_{\text{bin}}$ and BCT-based node features $\mathbf{X}_{\text{bct}}$ from fMRI data.
Preprocess SNP data and obtain genotype feature vectors $\mathbf{S}$.
Initialize the ICCO population within the search space Ω.
for $t = 1$ to $T_{\max}$ **do**
    for each candidate hyperparameter configuration $\mathbf{X}_i$ **do**
        Initialize Evo-TGSF using $\mathbf{X}_i$.
        Extract fMRI representation $\mathbf{v}_{\text{img}}$ using TA-GCN($\mathbf{A}_{\text{bin}}, \mathbf{X}_{\text{bct}}$).
        Extract SNP representation $\mathbf{v}_{\text{snp}}$ using GSI-Net($\mathbf{S}$).
        Fuse $\mathbf{v}_{\text{img}}$ and $\mathbf{v}_{\text{snp}}$ using ACM-GF to obtain $\mathbf{v}_{\text{final}}$.
        Predict class probabilities $\hat{\mathbf{y}} = \text{MLP}(\mathbf{v}_{\text{final}})$.
        Compute validation fitness Fitness($\mathbf{X}_i$)
    end for
    Select the best candidate $\mathbf{X}_{\text{best}}$ according to the validation fitness.
    Update the ICCO population.
end for
Retrain Evo-TGSF with the optimal hyperparameters $\mathbf{X}_{\text{best}}$.
Evaluate the optimized model on the test set.
return predicted labels $\hat{\mathbf{Y}}$ and the optimized Evo-TGSF model.

4 Experiments and Results

4.1 Data Description

4.1.1 Data Acquisition

In this study, brain imaging genomics data were obtained from the Alzheimer's disease neuroimaging initiative phase 2 (ADNI2) database[1]. The dataset included subjects from four diagnostic groups, including AD, early mild cognitive impairment (EMCI), late mild cognitive impairment (LMCI), and HC. Each participant provided multimodal neuroimaging and genomics data. Specifically, the imaging data comprised T1-weighted (T1w) structural MRI, field mapping data, and fMRI. In addition, SNP data were acquired using the Human 610-Quad BeadChip platform [29]. Detailed information about the dataset was provided in Table 2.

[1] http://adni.loni.usc.edu

Table 2 Detailed information of the ADNI2 imaging–genomics dataset

Diagnosis	HC	EMCI	LMCI	AD
Number	26	45	25	24
Age (mean ± SD)	75.2 ± 6.0	71.0 ± 6.8	70.5 ± 7.1	72.5 ± 7.8
Male : Female	14 : 12	20 : 25	16 : 09	13 : 11

4.1.2 Data Preprocessing

We preprocessed the two omics datasets separately, including fMRI brain imaging data and SNP genomics data, using standardized pipelines to ensure data quality and consistency.

- **fMRI Data Preprocessing**. For fMRI brain imaging data preprocessing, a standardized pipeline was adopted to ensure rigorous quality control. First, fMRI data were spatially normalized and aligned to the human connectome project multi-modal parcellation (HCPMMP) atlas using the J-HCPMMP method [30], dividing each subject's brain into 360 regions of interest (ROIs). Using the fMRI data from these 360 brain parcellations, the functional connectivity strength between brain regions was calculated to generate a 360×360 brain connectivity matrix. Specifically, the mean BOLD time series of each ROI was extracted, and Pearson correlation coefficients were calculated between all pairs of ROIs to construct the weighted functional connectivity matrix. The absolute values of all correlation coefficients in the connectivity matrix were then used to eliminate the influence of negative correlations, while preserving the weighted network containing nodal connection information. Subsequently, the weighted connectivity matrix was binarized to generate an undirected binary adjacency matrix for graph-based analysis.
- **SNP Data Preprocessing**. For SNP data preprocessing, stringent quality control (QC) and imputation procedures were applied to ensure data accuracy and reliability [9]. Genotyping was performed using the human 610-Quad BeadChip platform. During preprocessing, samples and SNP markers with missing rates exceeding 5% were removed. Sex consistency was verified using X-chromosome markers, and samples with mismatched genetic and recorded sex information were excluded. Genetic relatedness among subjects was assessed based on identity-by-descent (IBD) coefficients, and one individual from each related pair (IBD > 0.125) was removed to minimize familial bias. Hardy–Weinberg equilibrium (HWE) testing was conducted for each SNP, with markers showing significant deviation ($p < 1 \times 10^{-6}$) discarded. In addition, SNPs with minor allele frequency (MAF) lower than 0.01 were excluded to reduce the influence of rare variants. After QC filtering, genotype imputation was performed using MACH software with an international human reference panel, retaining imputed variants with confidence scores $r^2 > 0.3$. Finally, the processed genotype data were standardized and converted into PLINK format, including consistent genotype encoding and genomic position annotation, to facilitate downstream imaging–genomics analysis. After quality control and preprocessing, genome-wide association analysis was performed on 120 subjects from the ADNI2 cohort using GAPIT3. SNPs were filtered based on minor allele frequency (MAF < 0.05) using

PLINK. Both generalized linear models (GLM) and mixed linear models (MLM) were applied to identify Alzheimer's disease–related variants ($p < 0.05$). The intersection of GLM- and MLM-derived results yielded 2,318 shared SNPs, which were retained for subsequent analyses.

4.2 Experimental Setting

The experimental evaluations were carried out on a workstation equipped with a Mac M2 Max and 32 GB of RAM under macOS 13.5, and all algorithms were implemented in Python using PyTorch. All comparative methods were implemented within the same experimental environment. To ensure a fair comparison, all competing methods were evaluated using the same 10-fold cross-validation splits, the same SNP feature set, and the same fMRI and SNP preprocessing pipeline as the proposed method. For Evo-TGSF model training, AdamW was adopted as the optimizer, with a batch size of 32, a dropout rate of 0.3, and a maximum of 100 training epochs. The random seed was fixed to 42 to improve experimental reproducibility. In the ICCO-based hyperparameter optimization process, the population size was set to 30 and the maximum number of iterations was set to 1000. The key hyperparameter settings of Evo-TGSF framework were summarized in Table 3.

Table 3 Hyperparameters settings of Evo-TGSF

Hyperparameter	Setting
Optimizer	AdamW
Number of attention heads	4
Dropout rate	0.3
Random seed	42
Batch size	32
Max training epochs	100
Population size of ICCO	30
Maximum iterations of ICCO	1000

4.3 The Experimental Results of the Proposed ICCO on Benchmark Functions

To verify the effectiveness of the proposed ICCO algorithm, its convergence performance, global exploration, and local exploitation capabilities were evaluated using the CEC 2017 benchmark functions. Furthermore, the performance of ICCO was compared against nine state-of-the-art optimization algorithms, including dung beetle optimizer (DBO) [31], harris hawks optimization (HHO) [32], sparrow search algorithm (SSA) [33], subtraction average–based optimizer algorithm (SABO) [34], sand cat swarm optimization (SCSO) [35], crested porcupine optimization (CPO) [36], red-billed blue magpie optimizer (RBOM) [37], and the original CCO. For all competitive algorithms,

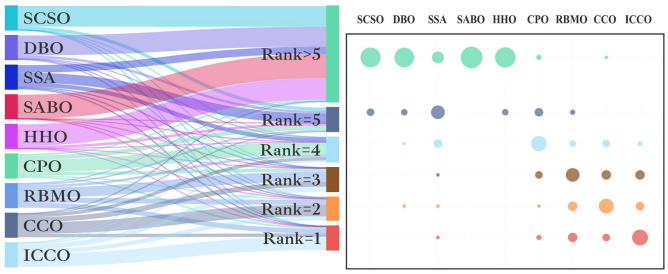
the population size was set to $N = 30$, the dimension to $Dim = 30$, and the maximum number of iterations to $T = 1000$. Detailed key parameters for all optimization algorithms are provided in Table 4.

Table 4 Comparison of algorithm parameters

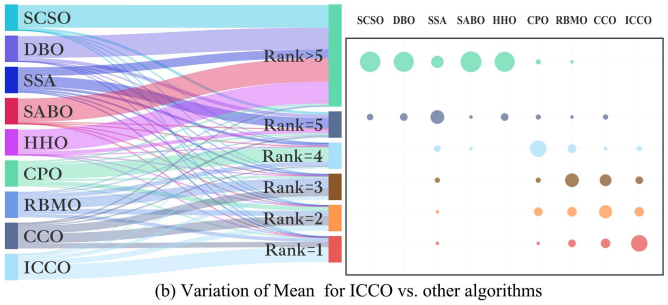
Algorithms	Parameter values
DBO	$k \in (0, 0.02]$, $b \in (0, 1)$, $\alpha \in [-1, 1]$;
SSA	$v_0 = 0$, $\alpha \in (0, 1]$, $R_2 \in [0, 1]$, ST $\in [0.5, 1.0]$;
SABO	$r_{i,d} \in [0, 1]$;
HHO	$r \in (0, 1)$, $u \in [0, 1]$, $v \in [0, 1]$, $\beta = 1.5$;
CPO	$T_c = 2$, $T_f = 0.8$, $\beta = 0.8$;
SCSO	SM = 2, Roulette wheel selection $\in [0, 360]$;
RBMO	$\varepsilon = 0.5$;
CCO	$\alpha = 1.34$, $\beta = 1.5$;
ICCO	$\alpha = 1.34$, $\beta = 1.5$;

To rigorously evaluate the performance of the ICCO algorithm, comparative experiments were conducted using the CEC 2017 benchmark functions [38]. The performance of nine optimization algorithms was assessed based on Best, Mean, and Standard Deviation (Std) metrics, with the superior results highlighted in bold. The results presented in the table indicated that ICCO exhibited outstanding performance on multiple benchmark functions. In particular, ICCO achieved superior fitness values compared with the other algorithms on functions F4, F8, F9, F11, F12, F14, F16, F18, F22, F23, F28, F29, and F30, demonstrating its strong optimization capability across diverse problem landscapes. For unimodal benchmark functions, such as F1–F3, the primary evaluation focused on the exploitation ability of the algorithms, since only a single global optimum exists. ICCO consistently achieved favorable best results on F1 function, demonstrating effective local search performance and fast convergence behavior. In multimodal benchmark functions F4–F10, which contain multiple local optima, ICCO exhibited clear advantages in terms of best or mean values on several functions, particularly F4, F6, F7, F8, F9 and F10. These results indicated that ICCO maintained sufficient population diversity during the search process, enabling it to avoid premature convergence and escape local optima effectively. For hybrid and composition benchmark functions F11–F30, which were characterized by complex landscapes and strong variable interactions, ICCO continued to outperform the comparative algorithms on most functions. Notably, ICCO achieved the optimal or near-optimal results on F11, F12, F14, F16, F18, F22, F23, F28, F29 and F30, reflecting its robustness and strong global optimization capability under high-dimensional and nonlinear conditions.

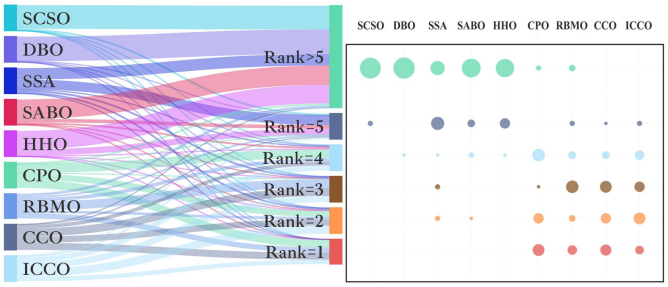
Figure 2 presented the ranking Sankey and ranking Bubble Charts, providing a clear comparative analysis of ICCO and eight other optimization algorithms according to Best, Mean, and Std results. The performance was evaluated across six ranking categories, including $Rank = 1$, $Rank = 2$, $Rank = 3$, $Rank = 4$, $Rank = 5$



(a) Variation of Best for ICCO vs. other algorithms



(b) Variation of Mean for ICCO vs. other algorithms



(c) Variation of Std for ICCO vs. other algorithms

Fig. 2 The ranking Sankey and ranking Bubble Chart of nine optimization algorithms.

and $Rank > 5$. From Figure 2, the combined Sankey diagrams and bubble charts revealed that ICCO consistently achieved a higher proportion of $Rank = 1$ and $Rank = 2$ results across all evaluation criteria. This demonstrated its strong capability in obtaining high-quality solutions as well as maintaining stable average performance. In contrast, the ranking distributions of HHO, SABO, SSA, DBO and SCSO were mainly concentrated in $Rank = 5$ and $Rank > 5$, indicating relatively inferior optimization accuracy and robustness. Meanwhile, CPO, RBMO, and CCO generally maintained rankings within the top four positions, suggesting that these three optimization algorithms also possessed competitive optimization performance. Therefore, CPO, RBMO, and CCO were selected as representative comparison algorithms in the subsequent experiments.

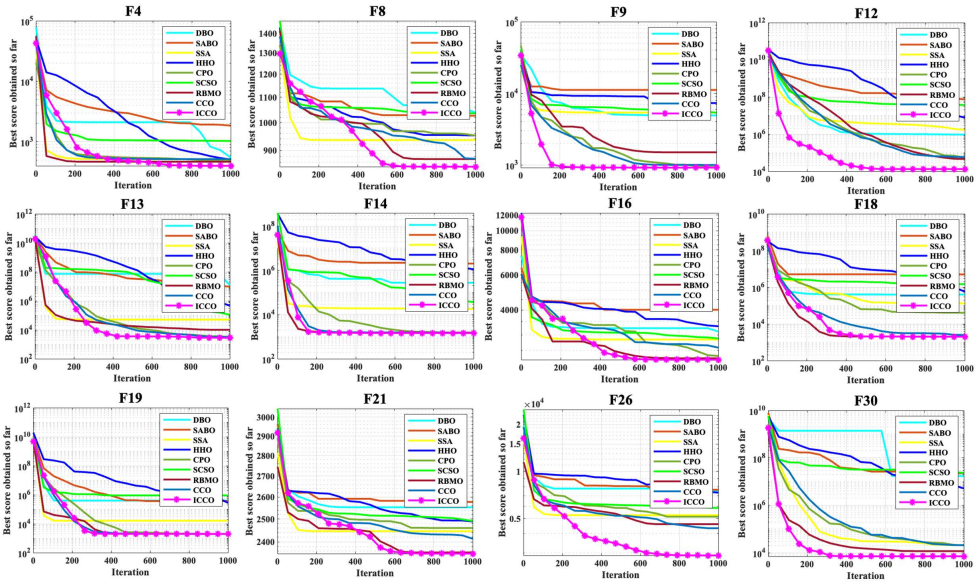


Fig. 3 Convergence curves of different optimization algorithms on CEC 2017.

Figure 3 illustrated the convergence curves of ICCO compared to nine state-of-the-art algorithms in selected benchmark functions of the CEC 2017 in F4, F8, F9, F12, F13, F14, F16, F18, F19, F21, F26 and F30. As observed from the plots, ICCO exhibited a significantly faster convergence rate in the initial iterations, which was particularly evident on functions F4, F12 and F26. These findings indicate that ICCO maintains a robust equilibrium between exploration and exploitation, resulting in superior convergence accuracy and stability across diverse fitness landscapes. Overall, ICCO consistently outperformed the state-of-the-art optimization algorithms. The enhanced performance is primarily driven by the synergy between the nonlinear dynamic capture factor, the elite differential mutation strategy, and the LOBL mechanism. These integrated strategies effectively preserve population diversity and refine the exploration–exploitation trade-off, enabling the algorithm to bypass local optima while accelerating the global convergence process.

The statistical merits of the proposed ICCO were assessed using the Wilcoxon rank-sum test relative to nine state-of-the-art algorithms. The resulting p-values, detailed in Supplementary Table A1 (with bold text marking values exceeding 0.05), revealed a clear trend: ICCO maintained a significant performance lead over the majority competitors. Since most p-values satisfy the $p < 0.05$ criterion, the data provided strong evidence of the unique optimization advantages of ICCO. This statistical disparity was not merely a numerical gain, it reflected the inherent structural superiority of the algorithm in the navigation of complex search spaces. By successfully avoiding premature convergence in local optima, ICCO consistently secured solutions of superior precision compared to the other methods evaluated.

4.4 The Experimental Results of the Proposed Evo-TGSF Framework

4.4.1 Classification Performance

We conducted five groups of AD classification tasks on the ADNI2 dataset, including HC/EMCI/LMCI, EMCI/LMCI/AD, HC/LMCI/AD, HC/EMCI/AD and HC/EMCI/LMCI/AD. A 10-fold cross-validation protocol was employed to ensure a rigorous evaluation of the proposed Evo-TGSF framework across multiple three-class and four-class diagnostic tasks. The dataset was divided into ten folds, with 9 subsets used for training and 1 subset for testing. This procedure was repeated ten times. As shown in Table 5, the metrics reported, including accuracy, precision and recall, represented the average performance across all folds, thus mitigating bias arising from random data partitioning and confirming the model's generalization capability. In general, the Evo-TGSF framework demonstrated stable and competitive performance across all tasks. Specifically, the model achieved average accuracies of roughly 82.1%, 92.2%, 88.7% and 83.4% for HC/EMCI/LMCI, HC/EMCI/AD, HC/LMCI/AD and EMCI/LMCI/AD groups, respectively, with balanced precision and recall values. Even in the four-way classification task, it secured a competitive accuracy of 80.2%.

Table 5 Classification performance of Evo-TGSF on three-class and four-class tasks.

Tasks	Accuracy	Precision	Recall
HC/EMCI/LMCI	82.1 ± 3.45	82.1 ± 2.55	80.7 ± 4.56
HC/EMCI/AD	92.2 ± 3.53	89.3 ± 2.63	92.0 ± 2.59
HC/LMCI/AD	88.7 ± 2.35	87.4 ± 3.61	90.0 ± 3.58
EMCI/LMCI/AD	83.4 ± 4.47	81.3 ± 3.55	83.0 ± 3.70
HC/EMCI/LMCI/AD	80.2 ± 4.57	80.1 ± 4.65	79.7 ± 5.23

4.4.2 Ablation Studies

To systematically evaluate the practical efficacy of the proposed multi-strategy ICCO algorithm within the context of AD assisted diagnosis, a series of ablation studies were designed and conducted. The primary objective of these experiments was to verify the independent contributions and synergistic effects of the three core strategic components, including NDCF, EDM and LOBL. By incrementally removing each strategy and comparing the resulting performance fluctuations across various classification tasks, the influence and optimization capacity of each mechanism on the overall model performance were quantitatively analyzed. The detailed experimental results were summarized in Table 6, illustrating the specific contribution of each strategy to global diagnostic performance.

As indicated in Table 6, the three proposed strategies generally contributed to improving the overall optimization performance of the model. NDCF introduced a cosine-based nonlinear decay mechanism to regulate the transition between global

exploration and local exploitation, thereby improving the stability of the search process. EDM enhanced population diversity by incorporating differential perturbations guided by elite individuals, which helped expand the search space and reduce the risk of premature convergence. LOBL further strengthened local refinement by generating lens-opposition candidate solutions around the current optimum, enabling the optimizer to escape local optima more effectively. Among the single-strategy ablations, removing LOBL caused a clear performance decline in the four-class task, with the accuracy decreasing to 75.5%, indicating its important role in maintaining robust local search ability. Moreover, variants with two strategies removed showed more pronounced performance degradation, with the lowest accuracy dropping to 72.9%. These results suggest that NDCF, EDM, and LOBL provide complementary benefits, and their integration enables ICCO to achieve a better balance between exploration and exploitation, resulting in more stable diagnostic performance across different classification tasks.

Table 6 Comparison results (%) of multi strategy ablation experiments.

w/o Strategies	HC/EMCI/LMCI	EMCI/LMCI/AD	HC/LMCI/AD	HC/EMCI/AD	HC/EMCI/LMCI/AD
w/o NDCF	**82.5 ± 1.35**	81.5 ± 5.34	85.3 ± 3.65	86.8 ± 2.31	77.4 ± 3.42
w/o EDM	81.4 ± 4.29	82.9 ± 3.26	86.2 ± 4.20	88.7 ± 2.50	78.2 ± 3.85
w/o LOBL	81.9 ± 3.32	80.8 ± 4.76	87.8 ± 3.74	90.7 ± 1.75	75.5 ± 2.52
w/o NDCF+EDM	81.3 ± 4.32	80.5 ± 1.36	84.3 ± 4.12	84.5 ± 2.46	75.9 ± 7.34
w/o LOBL+EDM	80.4 ± 6.43	78.7 ± 7.32	83.4 ± 3.76	83.9 ± 4.21	73.2 ± 2.29
w/o LOBL+NDCF	79.3 ± 2.36	80.3 ± 3.82	84.6 ± 4.72	85.2 ± 2.59	72.9 ± 3.22
ours	82.1 ± 3.45	**83.4 ± 4.47**	**88.7 ± 2.35**	**92.2 ± 3.53**	**80.2 ± 4.57**

We conducted an ablation study to verify the contribution of each component within the Evo-TGSF framework by constructing four variants, including w/o TA-GCN, w/o GSI-Net, w/o ACM-GF and w/o ICCO. As summarized in Table 7, the complete Evo-TGSF model consistently outperformed all degraded variants across all diagnostic settings. Most notably, in the challenging four-class classification task, the removal of the TA-GCN module precipitated a decline in accuracy from 80.2% to 58.8%. Additionally, the absence of ACM-GF precipitated a decline in accuracy to 62.5%, underscoring the necessity of the adaptive gating mechanism in managing multimodal heterogeneity. Similarly, the removal of ICCO results in a drop to 75.2%, substantiating its critical role in robust parameter optimization. These findings demonstrated that both components are essential for ensuring precise AD diagnosis and validating the synergistic design of the framework.

Table 7 Comparison results (%) of module ablation experiments.

w/o module	HC/EMCI/LMCI	EMCI/LMCI/AD	HC/LMCI/AD	HC/EMCI/AD	HC/EMCI/LMCI/AD
w/o TA-GCN	72.3 ± 6.55	68.7 ± 8.24	73.6 ± 2.45	62.2 ± 7.56	58.8 ± 9.27
w/o GSI-Net	78.7 ± 5.36	73.8 ± 7.65	79.6 ± 5.08	84.7 ± 3.53	73.4 ± 4.87
w/o ACM-GF	70.5 ± 7.45	68.4 ± 8.52	72.8 ± 5.48	76.3 ± 5.94	62.5 ± 7.30
w/o ICCO	81.3 ± 3.56	78.6 ± 5.87	83.3 ± 6.73	83.8 ± 1.24	75.2 ± 4.02
ours	**82.1 ± 3.45**	**83.4 ± 4.47**	**88.7 ± 2.35**	**92.2 ± 3.53**	**80.2 ± 4.57**

4.4.3 Comparison Results with Other Methods

The ICCO algorithm was employed within the Evo-TGSF framework for parameter optimization. Consequently, based on the comparative analysis of nine optimization algorithms discussed above, we selected CCO, RBMO and CPO as benchmark algorithms to conduct comparative experiments on three-class and four-class AD diagnostic tasks. All models were subjected to the same data processing pipeline as the Evo-TGSF framework using ICCO, with performance quantified using five distinct evaluation metrics. Furthermore, the mean and standard deviation were used as statistical measures to rigorously assess the classification efficacy and stability of each model in multi-class tasks, as illustrated in Figure 4. For the four classification tasks, the classification accuracies of CCO, RBMO and CPO are 76.7%, 75.4% and 73.6%, respectively. The experimental results demonstrated that, across all three evaluation metrics and four three-class tasks and one four-class task, the classification performance of the Evo-TGSF framework using ICCO significantly surpasses that of the comparative models. In addition, the classification accuracy of Evo-TGSF-ICCO was higher than that of Evo-TGSF-CCO, which demonstrated the effectiveness of the multi-strategy optimization method in AD diagnosis.

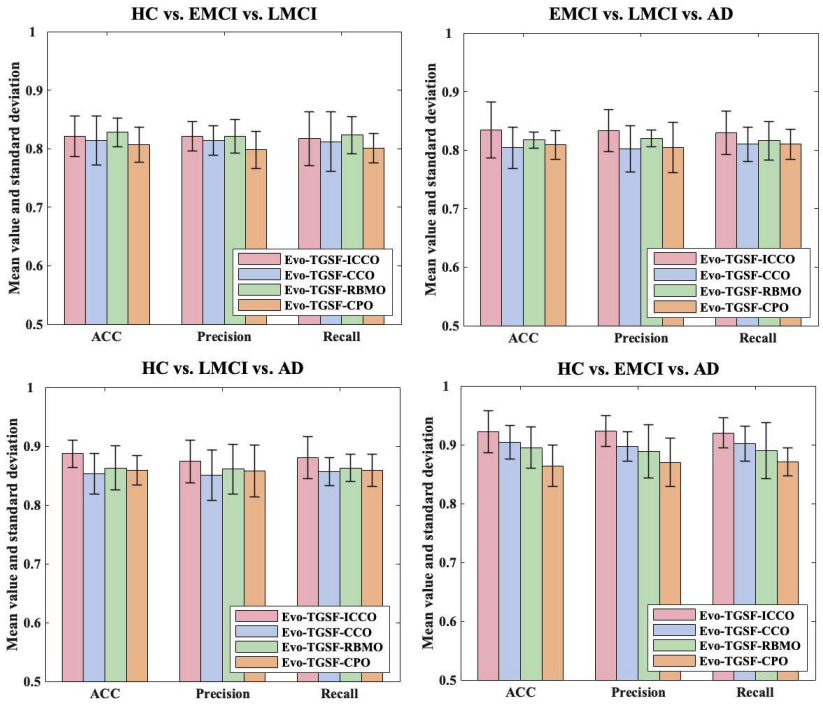


Fig. 4 Result of Evo-TGSF framework using different optimization algorithms for 3-class tasks in three indexes for performance evaluation.

To further evaluate the effectiveness of the proposed Evo-TGSF framework, several representative models were selected for comparative analysis, including CNN, GCN, AdaBoost, LDA, FusionNet-ISBOA-MK-SVM, and Concat-Fusion MLP. As shown in Table 8, the experimental results demonstrated that the proposed method consistently achieved superior performance across different three-class and four-class diagnostic tasks.

Table 8 Comparison results (%) of the proposed method and other algorithms.

Tasks	CNN	GCN	AdaBoost	LDA	FusionNet-ISBOA-MK-SVM	Concat-Fusion MLP	ours
HC/EMCI/LMCI	68.5	77.2	72.4	74.9	**83.3**	80.5	82.1
EMCI/LMCI/AD	72.8	78.4	76.3	67.6	80.5	75.6	**83.4**
HC/LMCI/AD	75.6	80.2	70.8	77.4	82.9	78.3	**88.7**
HC/EMCI/AD	70.2	82.5	68.9	70.9	85.4	80.1	**92.2**
HC/EMCI/LMCI/AD	62.5	70.7	58.3	60.8	75.6	68.5	**80.2**

In recent years, machine learning and deep learning methods had been widely applied in the auxiliary diagnosis of Alzheimer's disease. However, there were significant differences in dataset types, data modality selection, preprocessing processes, and feature selection methods in current research, resulting in a lack of unified comparison benchmarks between different research results. We selected references from the ADNI database with MRI and SNP data for three and four classification experiments for comparison in table 9. From the table, it can be seen that the proposed Evo-TGSF framework achieved better classification accuracy than other algorithms in multiple classification tasks. Specifically, in the challenging four-class classification task, our model achieved an accuracy of 80.2%, significantly outperforming the recent SS-SCSO-SVM method [18], which reported 72.0%. Compared to the CNN-BiLSTM approach [39] which relied on triple modalities (fMRI+sMRI+SNP), Evo-TGSF achieved higher accuracy (92.2% and 88.7%) using only dual modalities.

Table 9 Comparison of algorithm results with other researchers.

References	Methods	Data Modality	Tasks	ACC
Wang *et al.* [18]	SS-SCSO-SVM	fMRI+SNP	HC/EMCI/LMCI/AD	72.0%
Yan *et.al.* [39]	CNN-BiLSTM	fMRI+sMRI+SNP	HC/MCI/AD	86.0%
Xin *et al.* [40]	MDBO-SVM	sMRI+SNP	HC/MCI/AD	81.2%
Ours	Evo-TGSF	fMRI+SNP	HC/EMCI/LMCI	82.1%
			EMCI/LMCI/AD	83.4%
			HC/LMCI/AD	88.7%
			HC/EMCI/AD	92.2%
			HC/EMCI/LMCI/AD	80.2%

5 Discussion

Alzheimer's disease is intrinsically linked to aberrant neural activity and volumetric atrophy within specific neuroanatomical substrates governing memory, emotion, and higher-order cognition. These critical regions, encompassing the entorhinal cortex, hippocampus, prefrontal cortex, posterior cingulate cortex, angular gyrus, lateral parietal cortex, and anterior cingulate cortex, exhibit distinct spatiotemporal patterns of neurodegeneration across the progressive stages of cognitive impairment [41]. To further investigate the biological interpretability of the Evo-TGSF framework, we visualized the top-weighted brain regions identified across four distinct three-class classification tasks in Figure 5. The visualization revealed that while the feature distribution exhibits dynamic shifts corresponding to specific disease staging comparisons, there was a remarkable cross-task consistency among key pathological hubs. Among them, the 10d brain region was identified by the model as a key discriminative feature in all four three classification tasks. The recurrent identification of L_TF, L_STSvp and R_55b across three of the four three-class tasks underscores the multidimensional distribution of AD pathology within memory, perceptual and language networks [42, 43].

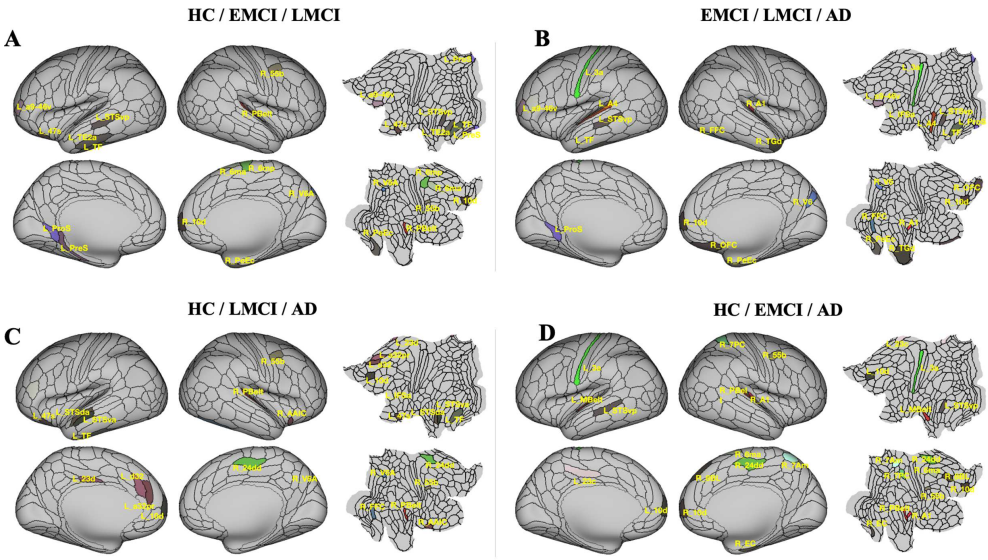


Fig. 5 Spatial distribution of discriminative brain regions identified across different three-class diagnostic tasks. In each panel, discriminative regions are displayed on the lateral, medial and ventral surfaces of the left and right hemispheres.

The observation of distinct yet partially overlapping discriminative regions across diverse classification scenarios underscores the stage-specific spatial patterns of neuropathological involvement. R_6mp, L_PreS and L_TE2a were exclusively identified

in the early-stage classification of HC/EMCI/LMCI. R_AAIC, L_STSva, L_STSda, L_a32pr and L_23d emerged uniquely in the HC/LMCI/AD task. R_OFC, R_TGd, R_V6 and L_A4 showed specific discriminative power for the pathological spectrum of EMCI/LMCI/AD. R_7PC, R_8BL, R_EC, L_MBelt, L_23c and R_7Am were distinct to the HC/EMCI/AD classification.

To further investigate the specific contributions of heterogeneous modalities to the disease staging process, we visualized the adaptive weights learned by the ACM-GF module. As illustrated in Figure 6, the adaptive gating mechanism consistently assigned higher weights to fMRI (0.60–0.75) compared to SNP (0.25–0.40) across all three-class and four-class diagnostic tasks. This distribution reflected the distinct nature of the modalities, fMRI captured dynamic functional phenotypes that directly correlated with progressive neurodegeneration, thereby serving as the primary discriminator for staging [44]. In contrast, SNP represented static genotypic susceptibility [13]. Despite being weighted lower, SNP data contributed significantly (weights > 0.25) by functioning as a stable genetic prior, thereby complementing imaging features. Therefore, the attention mechanism adaptively assigned dominance to the fMRI modality to maximize stage-discriminative power, while leveraging SNP data as a supportive genetic prior to ensure diagnostic stability.

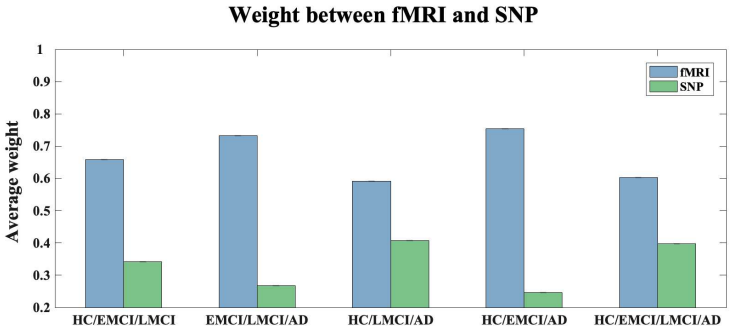


Fig. 6 The distribution of adaptive fusion weights between fMRI and SNP modalities across varying diagnostic tasks.

6 Conclusion

In this paper, we proposed Evo-TGSF model, a novel framework for precise AD classification using fMRI and SNP data. By synergizing topology-augmented GCN and genomic subspace interaction network, the framework effectively addressed binary network sparsity and non-linear genetic epistasis. These heterogeneous features are dynamically synthesized via adaptive cross-modal gated fusion. To improve hyperparameter optimization, we introduced the improved cuckoo-catfish optimizer, validated on CEC2017 benchmarks, to drive hyperparameter tuning. Extensive experiments on the ADNI dataset demonstrated that Evo-TGSF significantly outperformed state-of-the-art methods, exhibiting exceptional robustness in complex four-class classification.

Future work will address the challenges of longitudinal multi-modal data incompleteness and the scarcity of genotyped samples, aiming to establish a more resilient predictive model for tracking Alzheimer's disease progression over time.

Funding

This work is supported in part by the Humanitarian and Social Sciences Research Project of the Ministry of Education under Grant 24YJCZH278, in part by the 'Pioneer' and 'Leading Goose' R&D Program of Zhejiang under Grant 2024C04047.

Ethics declaration

This study used publicly available data from the ADNI database. All participants in ADNI provided informed consent under protocols approved by the relevant institutional review boards. No additional ethical approval was required for this secondary analysis.

Conflicts of Interet

The authors declare no conflicts of interest.

Appendix A Supplementary Table

References

[1] Wang, S., Jiao, C., Gao, Y., Cui, X., Wang, Y., Liu, J.: Deep association analysis framework with multi-modal attention fusion for brain imaging genetics. Medical Image Analysis, 103827 (2025)

[2] Xiang, S., Ling, H., Wu, M.: Cross-Modal alignment and rectified flow-based latent representation synthesis for enhanced speech-driven Alzheimer's disease detection. Bioengineering **13**(3), 370 (2026)

[3] Hechkel, W., Helali, A.: Unveiling Alzheimer's disease early: a comprehensive review of machine learning and imaging techniques. Archives of Computational Methods in Engineering **32**(1), 471–484 (2025)

[4] Wang, S., Liu, M., Li, Y., Zhang, X., Sun, M., Wang, Z., Li, R., Li, Q., Li, Q., He, Y., *et al.*: Recent advances in data-driven fusion of multi-modal imaging and genomics for precision medicine. Information Fusion **115**, 102738 (2025)

[5] Qiang, Y., Zhang, S., Li, J., Li, Y., Zhou, Q., Initiative, A.D.N., *et al.*: Diagnosis of Alzheimer's disease by joining dual attention CNN and MLP based on structural MRIs, clinical and genetic data. Artificial Intelligence in Medicine **145**, 102678 (2023)

Table A1 Experimental results of p-value Wilcoxon rank sum test for CEC 2017 benchmark functions

F	ICCO vs.							
	SCSO	DBO	SSA	SABO	HHO	CPO	RBMO	CCO
F1	3.02E-11	3.02E-11	1.11E-03	3.02E-11	3.02E-11	3.02E-11	3.02E-11	3.02E-11
F3	1.36E-07	4.57E-09	**9.47E-01**	1.73E-06	7.30E-04	3.02E-11	3.02E-11	3.02E-11
F4	3.03E-03	3.02E-11	1.29E-09	7.38E-10	3.34E-11	3.34E-11	3.34E-11	3.02E-11
F5	**1.71E-01**	**6.10E-01**	2.00E-06	**6.20E-01**	4.08E-11	3.02E-11	3.02E-11	3.02E-11
F6	3.99E-04	6.77E-05	8.65E-01	2.15E-02	3.02E-11	3.02E-11	3.02E-11	3.02E-11
F7	1.01E-08	1.56E-02	**3.18E-01**	1.60E-07	3.02E-11	3.02E-11	3.02E-11	3.02E-11
F8	**2.46E-01**	1.50E-02	2.15E-10	3.77E-04	5.97E-09	3.02E-11	3.02E-11	3.02E-11
F9	**3.33E-01**	4.03E-03	**5.11E-01**	4.11E-07	3.02E-11	3.02E-11	3.02E-11	3.02E-11
F10	**2.52E-01**	4.08E-05	3.69E-11	4.46E-01	3.37E-05	7.60E-07	**3.79E-01**	3.35E-08
F11	1.11E-04	3.02E-11	7.69E-08	3.69E-11	3.02E-11	3.02E-11	3.02E-11	3.02E-11
F12	1.49E-04	3.02E-11	2.39E-04	1.87E-07	3.02E-11	3.02E-11	3.02E-11	3.02E-11
F13	9.33E-02	1.78E-10	**8.50E-02**	**8.30E-01**	3.02E-11	3.34E-11	3.02E-11	3.02E-11
F14	3.39E-02	4.98E-04	1.68E-04	**9.05E-02**	3.02E-11	3.02E-11	3.02E-11	3.02E-11
F15	2.61E-02	3.47E-10	9.88E-03	**3.26E-01**	3.02E-11	3.02E-11	3.02E-11	3.02E-11
F16	**2.58E-01**	1.24E-03	2.23E-09	1.95E-03	4.44E-07	5.00E-09	1.41E-09	9.76E-10
F17	2.25E-04	**5.37E-02**	1.29E-09	6.20E-04	1.07E-09	3.52E-07	1.17E-09	4.31E-08
F18	**3.63E-01**	1.89E-04	**5.19E-02**	**4.12E-01**	2.15E-10	3.02E-11	3.02E-11	3.02E-11
F19	2.42E-02	4.08E-11	4.68E-02	**3.33E-01**	3.02E-11	3.02E-11	3.02E-11	3.02E-11
F20	**8.07E-01**	**5.01E-01**	5.60E-07	**1.15E-01**	6.70E-11	1.69E-09	1.09E-10	3.16E-10
F21	1.37E-03	**4.83E-01**	1.60E-07	6.05E-07	5.46E-09	3.34E-11	3.34E-11	3.69E-11
F22	3.64E-02	3.92E-02	**9.63E-02**	1.58E-04	3.02E-11	1.58E-01	3.02E-11	3.02E-11
F23	6.10E-03	**3.18E-01**	2.87E-10	1.55E-09	8.89E-10	1.61E-10	4.50E-11	5.49E-11
F24	7.29E-03	1.56E-02	2.39E-08	3.69E-11	5.07E-10	6.70E-11	3.02E-11	3.02E-11
F25	4.57E-09	3.02E-11	2.43E-05	3.02E-11	3.02E-11	3.02E-11	3.02E-11	3.02E-11
F26	**3.55E-01**	**5.89E-01**	5.60E-07	1.11E-03	1.16E-07	6.53E-08	1.41E-09	1.70E-08
F27	1.95E-03	1.55E-09	3.50E-03	4.03E-03	4.50E-11	4.50E-11	4.08E-11	3.02E-11
F28	2.01E-04	3.02E-11	3.09E-06	4.50E-11	3.02E-11	3.02E-11	3.02E-11	3.02E-11
F29	1.63E-02	4.12E-06	7.38E-10	**5.20E-01**	3.02E-11	3.69E-11	3.02E-11	3.34E-11
F30	9.51E-06	3.02E-11	1.22E-02	6.77E-05	3.02E-11	3.02E-11	3.02E-11	3.02E-11

[6] Jiao, C., Gao, Y., Ge, D., Shang, J., Liu, J.: Multi-modal imaging genetics data fusion by deep auto-encoder and self-representation network for Alzheimer's disease diagnosis and biomarkers extraction. Engineering Applications of Artificial Intelligence **130**, 107782 (2024)

[7] Rahman, M.J., Nipa, R.N.: Multimodal deep learning for Alzheimer's disease diagnosis: integrating neuroimaging and genetic data. Journal of Computer Science and Technology Studies **7**(2), 284–293 (2025)

[8] Peng, Y., Chen, K., Nie, F., Lu, B.-L., Kong, W.: Two-dimensional embedded fuzzy data clustering. IEEE Transactions on Emerging Topics in Computational Intelligence **7**(4), 1263–1275 (2022)

[9] Wang, L., Sheng, J., Zhang, Q., Song, Y., Zhang, Q., Wang, B., Zhang, R.: Diagnosis of Alzheimer's disease using FusionNet with improved secretary bird

optimization algorithm for optimal MK-SVM based on imaging genetic data. Cerebral Cortex **35**(2) (2025)

[10] Khazaee, A., Mohammadi, A., O'Reilly, R.: Multi-scale graph theoretical analysis of resting-state fMRI for classification of Alzheimer's disease, mild cognitive impairment, and healthy controls. Signal, Image and Video Processing **19**(14), 1192 (2025)

[11] Zhou, H., Liao, S., Guo, F.: TRIGCN: Graph convolution network based on tripartite graph for personalized medicine recommendation system. Systems **12**(10), 398 (2024)

[12] Chen, Y., Peng, Y., Tang, J., Camilleri, T., Camilleri, K., Kong, W., Cichocki, A.: EEG-based affective brain–computer interfaces: Recent advancements and future challenges. Journal of Neural Engineering **22**(3), 031004 (2025)

[13] Bae, J., Logan, P.E., Acri, D.J., Bharthur, A., Nho, K., Saykin, A.J., Risacher, S.L., Nudelman, K., Polsinelli, A.J., Pentchev, V., *et al.*: A simulative deep learning model of SNP interactions on chromosome 19 for predicting Alzheimer's disease risk and rates of disease progression. Alzheimer's & Dementia **19**(12), 5690–5699 (2023)

[14] Escott-Price, V., Hardy, J.: Genome-wide association studies for Alzheimer's disease: bigger is not always better. Brain Communications **4**(3), 125 (2022)

[15] Kamboh, M.I., Barmada, M.M., Demirci, F.Y., Minster, R.L., Carrasquillo, M.M., Pankratz, V.S., Younkin, S.G., Saykin, A.J., Sweet, R.A., Feingold, E., *et al.*: Genome-wide association analysis of age-at-onset in Alzheimer's disease. Molecular psychiatry **17**(12), 1340–1346 (2012)

[16] Cuyvers, E., Sleegers, K.: Genetic variations underlying Alzheimer's disease: evidence from genome-wide association studies and beyond. The Lancet Neurology **15**(8), 857–868 (2016)

[17] Lei, B., Zhu, Y., Yu, S., Hu, H., Xu, Y., Yue, G., Wang, T., Zhao, C., Chen, S., Yang, P.: Multi-scale enhanced graph convolutional network for mild cognitive impairment detection. Pattern Recognition **134** (2023)

[18] Wang, L., Sheng, J., Zhang, Q., Yang, Z., Xin, Y., Song, Y., Zhang, Q., Wang, B.: A novel sand cat swarm optimization algorithm-based SVM for diagnosis imaging genomics in Alzheimer's disease. Cerebral Cortex **34**(8) (2024)

[19] Peng, W., Li, C., Ma, Y., Dai, W., Fu, D., Liu, L., Liu, L., Yu, N., Liu, J.: Integrating time and frequency domain features of fMRI time series for Alzheimer's disease classification using graph neural networks. Interdisciplinary Sciences: Computational Life Sciences, 1–17 (2025)

[20] Bi, X.-a., Zhou, W., Luo, S., Mao, Y., Hu, X., Zeng, B., Xu, L.: Feature aggregation graph convolutional network based on imaging genetic data for diagnosis and pathogeny identification of Alzheimer's disease. Briefings in Bioinformatics **23**(3), 137 (2022)

[21] Sheng, J., Zhang, Q., Zhang, Q., Wang, L., Yang, Z., Xin, Y., Wang, B.: A hybrid multimodal machine learning model for detecting Alzheimer's disease. Computers in Biology and Medicine **170**, 108035 (2024)

[22] Zhang, Q., Sheng, J., Zhang, Q., Yang, Z., Xin, Y., Wang, B., Zhang, R., Initiative, A.D.N.: Optimizing deep learning with improved Harris Hawks optimization for Alzheimer's disease detection. Artificial Intelligence Review **58**(10), 301 (2025)

[23] Cui, X., Xiao, R., Liu, X., Qiao, H., Zheng, X., Zhang, Y., Du, J.: Adaptive LASSO logistic regression based on particle swarm optimization for Alzheimer's disease early diagnosis. Chemometrics and Intelligent Laboratory Systems **215**, 104316 (2021)

[24] Lu, D., Yue, Y., Hu, Z., Xu, M., Tong, Y., Ma, H.: Effective detection of Alzheimer's disease by optimizing fuzzy K-nearest neighbors based on salp swarm algorithm. Computers in Biology and Medicine **159**, 106930 (2023)

[25] Rubinov, M., Kötter, R., Hagmann, P., Sporns, O.: Brain connectivity toolbox: a collection of complex network measurements and brain connectivity datasets. NeuroImage **47**, 169 (2009)

[26] Hassan, N., Miah, A.S.M., Suzuki, K., Okuyama, Y., Shin, J.: Stacked CNN-based multichannel attention networks for Alzheimer disease detection. Scientific Reports **15**(1), 5815 (2025)

[27] Chelladurai, A., Narayan, D.L., Divakarachari, P.B., Loganathan, U.: fmri-based Alzheimer's disease detection using the SAS method with multi-layer perceptron network. Brain Sciences **13**(6), 893 (2023)

[28] Majumdar, P., Mitra, S.: Salp swarm algorithm using lens opposition-based learning and local search for constrained optimization problems. Iran Journal of Computer Science, 1–28 (2025)

[29] Bi, X.-a., Mao, Y., Luo, S., Wu, H., Zhang, L., Luo, X., Xu, L.: A novel generation adversarial network framework with characteristics aggregation and diffusion for brain disease classification and feature selection. Briefings in Bioinformatics **23**(6), 454 (2022)

[30] Sheng, J., Wang, B., Zhang, Q., Liu, Q., Ma, Y., Liu, W., Shao, M., Chen, B.: A novel joint HCPMMP method for automatically classifying Alzheimer's and different stage MCI patients. Behavioural brain research **365**, 210–221 (2019)

[31] Li, Y., Sun, K., Yao, Q., Wang, L.: A dual-optimization wind speed forecasting model based on deep learning and improved dung beetle optimization algorithm. Energy **286**, 129604 (2024)

[32] Alabool, H.M., Alarabiat, D., Abualigah, L., Heidari, A.A.: Harris hawks optimization: a comprehensive review of recent variants and applications. Neural computing and applications **33**(15), 8939–8980 (2021)

[33] Gharehchopogh, F.S., Namazi, M., Ebrahimi, L., Abdollahzadeh, B.: Advances in sparrow search algorithm: a comprehensive survey. Archives of Computational Methods in Engineering **30**(1), 427–455 (2023)

[34] Trojovskỳ, P., Dehghani, M.: Subtraction-average-based optimizer: A new swarm-inspired metaheuristic algorithm for solving optimization problems. Biomimetics **8**(2), 149 (2023)

[35] Seyyedabbasi, A., Kiani, F.: Sand cat swarm optimization: A nature-inspired algorithm to solve global optimization problems. Engineering with computers **39**(4), 2627–2651 (2023)

[36] Abdel-Basset, M., Mohamed, R., Abouhawwash, M.: Crested porcupine optimizer: A new nature-inspired metaheuristic. Knowledge-Based Systems **284**, 111257 (2024)

[37] Fu, S., Li, K., Huang, H., Ma, C., Fan, Q., Zhu, Y.: Red-billed blue magpie optimizer: a novel metaheuristic algorithm for 2d/3d UAV path planning and engineering design problems. Artificial Intelligence Review **57**(6), 134 (2024)

[38] Wu, G., Mallipeddi, R., Suganthan, P.N.: Problem definitions and evaluation criteria for the CEC 2017 competition on constrained real-parameter optimization. National University of Defense Technology, Changsha, Hunan, PR China and Kyungpook National University, Daegu, South Korea and Nanyang Technological University, Singapore, Technical Report **9**, 2017 (2017)

[39] Yan, Y.: A multimodal time-series model with adaptive attention mechanism for Alzheimer's disease classification. In: 2025 8th International Conference on Computer Information Science and Application Technology (CISAT), pp. 170–174 (2025). IEEE

[40] Xin, Y., Sheng, J., Zhang, Q., Song, Y., Wang, L., Yang, Z.: A novel diagnosis method utilizing MDBO-SVM and imaging genetics for Alzheimer's disease. Computerized Medical Imaging and Graphics, 102542 (2025)

[41] Tzavellas, N.P., Tsamis, K.I., Katsenos, A.P., Davri, A.S., Simos, Y.V., Nikas, I.P., Bellos, S., Lekkas, P., Kanellos, F.S., Konitsiotis, S., *et al.*: Firing alterations of neurons in Alzheimer's disease: are they merely a consequence of pathogenesis or a pivotal component of disease progression? Cells **13**(5), 434 (2024)

[42] Tsuchimine, S., Kudo, K., Komatsu, J., Shibata, S., Kitagawa, S., Misaka, Y., Noguchi-Shinohara, M., Ono, K., Morise, H., Asakawa, T.: Magnetoencephalographic brain activity evoked by the optic-flow task is correlated with β-amyloid burden and parahippocampal atrophy. NeuroImage: Clinical **44**, 103700 (2024)

[43] Zhang, Q., Fan, C., Wang, L., Li, T., Wang, M., Han, Y., Jiang, J.: Glucose metabolism in posterior cingulate cortex has supplementary value to predict the progression of cognitively unimpaired to dementia due to Alzheimer's disease: an exploratory study of 18F-FDG-PET. Geroscience **46**(1), 1407–1420 (2024)

[44] Arpanahi, S.K., Hamidpour, S., Jahromi, K.G.: Mapping Alzheimer's disease stages toward it's progression: A comprehensive cross-sectional and longitudinal study using resting-state fMRI and graph theory. Ageing Research Reviews **103**, 102590 (2025)